Journal of Hydrology 576 (2019) 370–380

Contents lists available at ScienceDirect

Journal of Hydrology

journal homepage: www.elsevier.com/locate/jhydrol

Research papers

Smoothed Particle Hydrodynamics modelling of fresh and salt water dynamics in porous media

Hossein Basser[a,*], Murray Rudman[b], Edoardo Daly[a]

[a] Department of Civil Engineering, Monash University, VIC 3800, Australia
[b] Department of Mechanical and Aerospace Engineering, Monash University, VIC 3800, Australia

ARTICLE INFO

This manuscript was handled by Huaming Guo, Editor-in-Chief, with the assistance of Fereidoun Rezanezhad, Associate Editor

Keywords:
Smoothed Particle Hydrodynamics (SPH)
Explicit Incompressible SPH (EISPH)
Freshwater lens
Upconing
Pumping
Porous media
Sink

ABSTRACT

Seawater intrusion modelling is often used to assist with groundwater management in coastal areas and islands. Although Smoothed Particle Hydrodynamics (SPH) schemes are able to simulate multi-fluid flows in porous media, they have not been widely tested against experimental observations yet. Additionally, numerical methods for groundwater flow problems need to be able to simulate pumping, which is an unexplored area in SPH. In this study, an Explicit Incompressible SPH (EISPH) solver for multi-fluid flow in porous media is used to simulate the dynamics of freshwater lenses in small islands, and is further developed to simulate groundwater pumping and associated seawater upconing. Three methods to implement a sink term that models water pumping from an aquifer are proposed and compared. The model is successfully tested against data from published laboratory-scale experiments and other numerical models. The results of EISPH are comparable to other models. The inclusion of a sink for water particles to simulate pumping did not affect the stability of the simulations, although one of the three methods led to results that better compared to experimental data. Hence, SPH modelling of groundwater flows in porous media can be successfully achieved using the methods developed here.

1. Introduction

Seawater intrusion in groundwater aquifers is a global issue that threatens availability of potable freshwater in coastal zones. A naturally occurring process, seawater intrusion is often enhanced by changes in fresh groundwater levels caused by pumping through extraction wells and land-use change (Werner et al., 2013). The change in groundwater levels causes reductions in the pressure exerted by overlying freshwater columns, leading to upward intrusion of underlying seawater (Bertorelle, 2014). The intrusion reduces freshwater storage volume and might contaminate freshwater extraction wells (Werner et al., 2013).

Seawater intrusion is also of great importance in oceanic islands, where fresh groundwater is often the only potable water source (Stoeckl and Houben, 2012). In oceanic islands, fresh groundwater often floats over underlying seawater due to the density difference. This floating body of freshwater is called a lens (Stoeckl and Houben, 2012; Stoeckl et al., 2016). Freshwater lenses in oceanic islands often have limited thickness and are separated from the underlying seawater by a mixing zone. Dynamics of the mixing zone at the interface between freshwater and seawater are governed by a density-dependent multi-fluid flow (Werner et al., 2017). Factors associated with changes in rainfall regimes and excessive pumping of freshwater can reduce the thickness of these lenses as well as increase the possibility of seawater intrusion to extraction wells (Stoeckl and Houben, 2012; Werner et al., 2017).

To investigate the process of seawater intrusion and understand the vulnerability of fresh groundwater aquifers, numerous methods such as field monitoring techniques, analytical studies, and numerical models have been developed (Werner et al., 2013). Field techniques, such as direct sampling and remote sensing (White, 1996), are used as the basis for empirical equations (Werner et al., 2017). Analytical solutions have been developed to predict the position of an interface between freshwater and seawater. These methods mostly assume a sharp interface between two immiscible fluids and are derived for simplified steady-state conditions in homogeneous aquifers (Vacher, 1988; Fetter, 1972; Dagan and Bear, 1968). Numerical methods have been developed to overcome the limitations of analytical solutions and are able to model transient development of the interface of miscible fluids in aquifers with spatial hydraulic heterogeneity. Numerical models mostly solve a variable density multi-fluid flow coupled with a solute transport equation (Werner et al., 2013). The most commonly used codes are SUTRA (Voss et al., 2002) and SEAWAT (Langevin et al., 2008), which solve the equations using finite-elements and finite differences, respectively. Readers are referred to Werner et al. (2013, 2017) for a

* Corresponding author.
E-mail address: hosseinbasser@gmail.com (H. Basser).

https://doi.org/10.1016/j.jhydrol.2019.06.048
Received 30 October 2018; Received in revised form 26 May 2019; Accepted 17 June 2019
Available online 22 June 2019
0022-1694/

comprehensive review of common analytical and numerical studies.

Recently, particle methods, such as Smoothed Particle Hydrodynamics (SPH), have been used to simulate multi-fluid flow in porous media, with applications to lock-exchange (Basser et al., 2017; Pahar and Dhar, 2017). Particle methods have been shown to have performance similar to conventional mesh-based methods, with the advantage to reduce numerical diffusivity (Herrera et al., 2009). The modelling of anisotropic dispersion of solutes is one of the challenges faced by SPH schemes, with effort being dedicated to the reduction of the occurrence of negative concentrations (Avesani et al., 2015, 2017). However, the use of SPH schemes for the modelling of solute dispersion against experimental data are still rare. Further quantitative studies with applications to engineering problems are required to test the capability of SPH to simulate multi-fluid flow in porous media. Specifically, the simulation of problems including pumping from wells requires modelling a mass sink. One of the challenges associated with simulating a mass sink is tracking the particles around the sink point to ensure a well organised distribution of the particles, to ensure an accurate SPH approximation. Another challenge is defining how to remove mass associated with the extracted freshwater.

The aim of this study is thus to investigate the applicability of an SPH scheme, Explicit Incompressible SPH (EISPH) (Basser et al., 2017), to simulate freshwater lens formations in islands and sea water upconing due to pumping. An algorithm to simulate point mass sinks was developed and is presented here with applicability to water pumping.

2. Methods

2.1. Governing equations

The 2D governing equations for a flow of two or more incompressible fluids in saturated porous media, at the Darcy's scale, with mass sinks and solute transport are (Basser et al., 2017; Bear and Bachmat, 2012)

$$\nabla\cdot\vec{u} = -\Gamma, \tag{1}$$

$$\frac{D\vec{u}}{Dt} = -\frac{\epsilon}{\rho}\nabla p + \frac{\mu}{\rho}\nabla^2\vec{u} + \epsilon\,\vec{g} + \vec{R}, \tag{2}$$

$$\frac{DC}{Dt} = \nabla\cdot(\mathscr{D}_d\nabla C), \tag{3}$$

where Eqs. (1)–(3) define mass, momentum and species conservation, respectively, $\frac{D}{Dt}$ is the total derivative, $\vec{u}$ is the Darcian velocity equal to $\epsilon\,\vec{u}_f$, $\vec{u}_f$ being the fluid intrinsic velocity and ϵ porosity, Γ is a flux per unit of volume due to point sinks, p is pressure, μ is the dynamic viscosity, ρ is the density, $\vec{g}$ is the gravitational acceleration, $\vec{R}$ is the drag force imposed by porous media, C is scalar (salt here) concentration, and $\mathscr{D}_d$ is the effective dispersion matrix of size 2 for the scalar (see Appendix A).

2.2. SPH approximation

In SPH, the fluid domain is represented as an ensemble of Lagrangian particles. The values of variables associated with each particle are estimated using neighbouring particles. Readers are referred to Monaghan (1992, 1994, 2012) for a general description of the particle approximation; only key features of the model used in this study are presented here. The spatial volume, V, of particles in porous media with spatially varying porosity is determined in accordance with the porosity of the media, such that, when a particle moves into a medium with lower porosity, the same amount of mass occupies a larger volume (i.e., $V_i = m_i/(\epsilon_i\,\rho_i)$, where m is the fluid mass of the particle and i refers to the ith particle) (Basser et al., 2017; Pahar and Dhar, 2016).

The particle approximation of the governing equations reads (Monaghan, 2005; Tran-Duc et al., 2016; Basser et al., 2017)

$$\nabla\cdot\vec{u}_i = \sum_{j=1}^{N}\frac{m_j}{\epsilon_j\,\rho_j}(\vec{u}_j - \vec{u}_i)\cdot\nabla_i W_{ij} = -\Gamma_i, \tag{4}$$

$$\frac{D\vec{u}_i}{Dt} = \epsilon_i\sum_{j=1}^{N}\frac{m_j}{\epsilon_j}\left(\frac{p_i}{\rho_i^2}+\frac{p_j}{\rho_j^2}\right)\nabla_i W_{ij} + \sum_{j=1}^{N}\frac{4m_j(\mu_i+\mu_j)\vec{u}_{ij}\cdot\vec{x}_{ij}}{\epsilon_j\,(\rho_i+\rho_j)^2(|\vec{x}_{ij}|^2+\eta^2)}\nabla_i W_{ij} + \epsilon_i\,\vec{g} + \vec{R}_i, \tag{5}$$

with

$$\vec{R}_i = -\frac{\epsilon_i\,\mu_i}{\rho_i\kappa_i}\vec{u}_i, \tag{6}$$

$$\frac{DC_i}{Dt} = 2\sum_{j=1}^{N}\frac{m_j}{\epsilon_j\,\rho_j}\left(\frac{e_{ij,1}^2}{\bar{\mathscr{D}}_{dij,11}}+\frac{e_{ij,2}^2}{\bar{\mathscr{D}}_{dij,22}}\right)^{-1}\frac{\vec{x}_{ij}\cdot\nabla_i W_{ij}}{|\vec{x}_{ij}|^2+\eta^2}(C_i - C_j), \tag{7}$$

where i and j refer to the ith and jth particles, κ is the permeability of the medium, assumed to be constant, e_{ij} is a unit vector from i to j, $\bar{\mathscr{D}}_{dij}$ is the average of the effective dispersion matrices of particles i and j, the numbers in subscript of e_{ij} and $\bar{\mathscr{D}}_{dij}$ reference a particular element in the vector and the matrix, respectively. Eq. (6) equals zero where there is no porous medium.

The EISPH method was used to solve Eqs. (1)–(3) (Nomeritae et al., 2016); a detailed description of the numerical scheme used here is presented in Appendix A.

2.3. Modelling a point sink

To carry out SPH simulations of problems including water extraction through wells, a method to describe a sink for the extraction of water mass must be developed.

In a point sink, such as suction or pumping acting at a point, the fluid surrounding the sink point moves toward the sink point. In SPH, this means that fluid particles should move toward the sink point and a portion of the fluid's mass should be removed at a rate equal to the sink rate. The extraction of the mass from a point is included in Eq. (1) (Bear and Bachmat, 2012) in the form of fluid flux per unit of volume, Γ, and is approximated as

$$\Gamma = \sum_{k=1}^{s} Q_k\,\delta(\vec{x} - \vec{x}_k), \tag{8}$$

where k is the kth sink point, s denotes the number of sink points, Q is the sink rate and $\delta(\cdot)$ is the Dirac function. Eq. (8) describes fluid flux per unit volume due to sinks. The contributions of sinks for particle i is approximated as

$$\Gamma_i = \sum_{k=1}^{s} Q_k\,\delta(\vec{x}_i - \vec{x}_k) \approx \sum_{k=1}^{s} Q_k\,\zeta_k\,W_{ik}, \tag{9}$$

where ζ is a normalization factor equivalent to an approximation of constant 1 and defined as (Monaghan, 2005; Monaghan et al., 2005)

$$\frac{1}{\zeta_k} = \sum_{j=1}^{N}\frac{m_j}{\epsilon_j\,\rho_j}W_{jk}. \tag{10}$$

In Eq. (9), sink points within a distance equal to the radius of the support of the kernel function from particle i are used to calculate Γ; therefore, a sink point directly affects the particles (sink particles hereafter) within a distance equal to the radius of the support domain of the kernel function from the sink point. The particles outside the direct influence of the sink point are indirectly affected through their interaction with the sink particles.

The term Γ contributes to the pressure Poisson equation (Eq. (21)), causing the pressure of the particles surrounding the sink point to change in a way that they move towards the sink point.

Each particle in SPH carries a certain amount of fluid mass and in order to account for the mass extraction due to the sink, it is

unavoidable to reduce the particles mass and delete particles where and when necessary. Three different methods for deleting particles are proposed to investigate their advantages and disadvantages.

2.3.1. Solely Particle Removal (SPR)

In this method, the mass reduction due to the sink is handled by just deleting particles, while maintaining the total particle mass constant in between deletion. Individual particle mass still needs to be updated due to changes in scalar concentration according to Eq. (7). One particle is deleted after a certain number of time steps. The duration, t_p, required to delete one particle is determined using the volume of fluid in a particle and the sink rate, such that

$$t_p = \frac{\epsilon V}{Q}, \tag{11}$$

where V is a spatial volume (Section 2.2) associated with a particle, and ϵV is the volume of fluid that each particle carries. Mass is reduced (i.e., one particle is removed) at every time step that is a multiple of t_p (i.e., at times $t = \alpha t_p$, α being an integer). Every time $t = \alpha t_p$, the particle closest to the sink point is removed (Fig. 1a).

Because the sink particles move toward the sink point due to the inclusion of Γ in the pressure Poisson equation (Eq. (21)), the particle deletion does not lead to a void in the vicinity of the sink point.

2.3.2. Mass Reduction and Particle Removal (MRPR)

Similar to *SPR*, one particle is removed every certain number of time steps. However, in contrast to *SPR*, the mass of sink particles is gradually reduced every time step before one particle is deleted. The amount of mass reduction in one time step is divided among the sink particles and subtracted from each sink particle's mass. The mass required to be removed is partitioned between sink particles in two ways: (1) in accordance to the kernel value ($MRPR_K$), so that the particles closer to a sink point lose more mass than the distant ones, or (2) evenly ($MRPR_E$). Therefore, the amount of mass extracted from each particle is determined using the sink rate, time step value, kernel value (used in $MRPR_K$), and number of sink particles (used in $MRPR_E$). When the time required to delete one particle, αt_p, is reached, the closest particle to the sink point is removed and the mass of the remaining sink particles is set back to their initial mass value (Fig. 1b).

2.3.3. Constant Mass Reduction (CMR)

In this method, the mass of the sink particles is gradually reduced every time step, as in $MRPR_E$. The reduction in mass of the sink particles continues until the mass of a sink particle drops below a cut-off value, which here is set to 1% of particles initial mass value, at which time the particle is removed (Fig. 1c). The reduction of mass in accordance to the kernel value (as in $MRPR_K$) was found problematic as continuous reduction of particles mass causes clumping of particles close to a sink point; this is further explained in Section 3.2.

2.4. Choice of kernel

The selection of a kernel function and smoothing length in a problem in media with different porosities should be handled carefully. The spatial volume that an SPH particle occupies within a porous medium represents both fluid and solid phases volume. Therefore, a

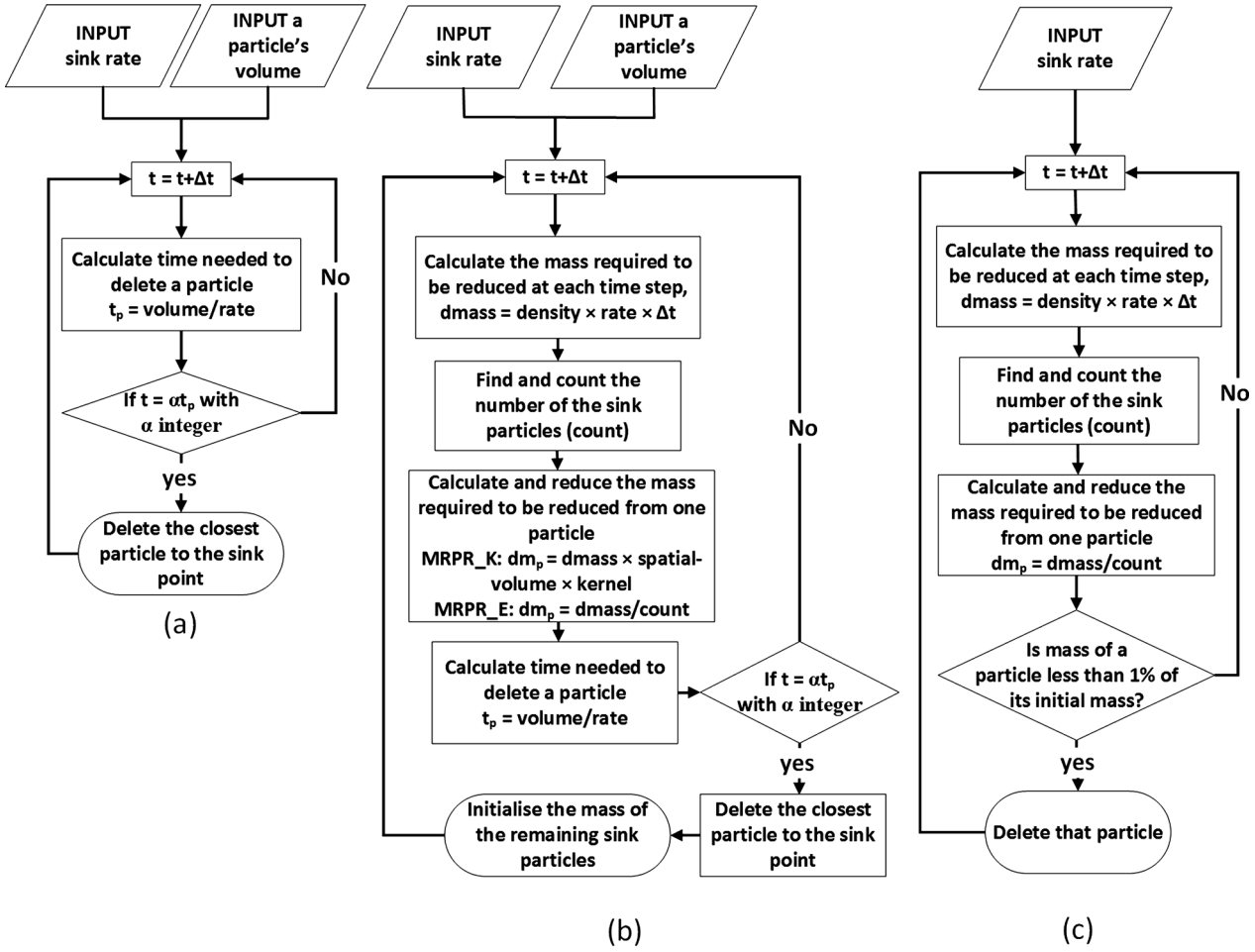

Fig. 1. The procedure for the reduction of mass due to a sink point using (a) Solely Particle Removal (SPR) (Section 2.3.1), (b) Mass Reduction and Particle Removal (MRPR) (Section 2.3.2) and (c) Constant Mass Reduction (CMR) (Section 2.3.3).

fluid particle with a given mass within a porous medium has a larger spatial volume than a particle in a free flow domain with the same mass. Having a larger spatial volume causes the particles to move apart from each other, leading to a loss of resolution inside the porous medium. Therefore, the number of particles inside the support domain of the kernel function reduces and might not be sufficient to accurately approximate the variable values and derivatives. To tackle this problem, a kernel function with a larger support domain should be used or the smoothing length should be adjusted (Pahar and Dhar, 2016). The former approach might lead to an excessive smoothing of the variable values at the free flow domain. Furthermore, using a larger support domain increases the number of interactions in the free flow domain, leading to a higher computational cost. Here we use a variable smoothing length. Additional terms associated with the derivative of smoothing length are added to the momentum equation (Price and Monaghan, 2004); however, these terms are neglected here.

A cubic spline weighting function (Liu and Liu, 2003), with a variable smoothing length, was used here and is given by

$$W(q, h) = \alpha_d \times \begin{cases} \frac{2}{3} - q^2 + \frac{1}{2}q^3 & 0 \leqslant q < 1 \\ \frac{1}{6}(2-q)^3 & 1 \leqslant q < 2 \\ 0 & q \geqslant 2, \end{cases} \tag{12}$$

where α_d is a normalisation constant equal to $1/h$, $15/(7\pi h^2)$, or $3/(2\pi h^3)$ in one-, two- and three-dimensional domains, respectively, and $q = |\vec{x_i} - \vec{x_j}|/h = |\vec{x}_{ij}|/h$. In 2D, we choose the smoothing length to be inversely proportional to the square root of porosity as

$$h_i = 1.2\frac{\Delta x}{\sqrt{\epsilon_i}}, \tag{13}$$

where Δx is the average distance between fluid particles; therefore, in a medium with lower porosity the smoothing length is larger.

Because the same value of smoothing length should be used for a pair of interacting particles to conserve momentum, the smoothing length for interacting particles i and j is calculated as $h_{ij} = (h_i + h_j)/2$ (Rafiee et al., 2007).

2.5. Boundaries

2.5.1. Solid boundaries

A single layer of virtual particles is used to impose the impermeable boundaries at walls. Virtual particles interact with fluid particles and prevent them from penetrating the walls by exerting a Lennard-Jones repulsive force given by Monaghan (1994)

$$F(\vec{x})_{ij} = \begin{cases} V_L \left[\left(\frac{r_c}{|\vec{x}_{ij}|}\right)^{c_1} - \left(\frac{r_c}{|\vec{x}_{ij}|}\right)^{c_2} \right] \frac{1}{|\vec{x}_{ij}|} & \frac{r_c}{|\vec{x}_{ij}|} \geqslant 1, \\ 0 & \frac{r_c}{|\vec{x}_{ij}|} < 1, \end{cases} \tag{14}$$

with c_1 and c_2 equal to 4 and 2 respectively, V_L is the square of the largest velocity in a flow, and r_c represents a cut off distance which is set to 0.8 times the initial distance between virtual particles. The virtual particles are fixed in their position and never move. The initial distance between the virtual particles is set to half the initial distance between the fluid particles to ensure the impermeability of the walls.

2.5.2. Free/no-slip boundaries

Ghost particles are used to impose free-slip and no-slip boundary conditions. Ghost particles are created by mirroring the fluid particles within a distance of 2 h from the solid boundaries (Liu and Liu, 2003). A ghost particle carries the same properties of the associated fluid particle. To impose no-slip boundary condition both components of velocity, parallel and normal, are reversed, while for free-slip conditions only the normal component is reversed (Marrone et al., 2011). Our investigations and previous studies (e.g. Nomeritae et al., 2016; Basser et al., 2017) showed that ghost particles alone were not able to prevent particles from penetrating the solid walls; therefore, the ghost particles were used together with the virtual particles.

2.5.3. Inflow boundaries

Inflow particles are used to simulate inflow of fluid into the domain (Nomeritae et al., 2018). The thickness of the zone occupied by inflow particles, i.e., the inflow zone, is set to be larger than the radius of the support domain of the kernel function. Inflow particles within the inflow zone are moved with a constant velocity determined by the inflow rate. Once an inflow particle moves outside the inflow zone, it is turned into a fluid particle and moves according to the governing equations. The inflow particles' velocity and pressure are used in approximating the hydrodynamics of the fluid particles in a domain but not vice versa (Federico et al., 2012).

2.5.4. Free surface boundaries

A pressure $p = 0$ is assigned to free surface particles. The free surface particles are detected using fluid particles' densities as in Basser et al. (2017).

3. Results

The model is applied to two experimental studies to test different aspects of the method and validate it. The experimental coastal freshwater lens in an isotropic porous medium studied in Stoeckl and Houben (2012) is simulated to check the capability of the model to reproduce the dynamics of fresh and salt water in a porous medium. The experiment of salt water upconing induced by fresh water pumping studied in Werner et al. (2009) was simulated to validate the proposed sink algorithm and demonstrate the capability of the SPH scheme to reproduce upconing of salt water in groundwater aquifers.

3.1. Laboratory-scale coastal freshwater lens

An experiment of formation of a coastal freshwater lens in a cone shape strip island was presented in Stoeckl and Houben (2012). In the experiment, a cone shape submerged island 1.8 m long, 0.3 m deep, and 0.05 m wide was utilized (Fig. 2). The porosity and mean hydraulic conductivity of the porous medium were given as $\epsilon = 0.39$ and $K = 4.5 \times 10^{-3}$ m s^{-1}, respectively. The salt and fresh water densities were $\rho_s = 1021.2$ kg m^{-3} and $\rho_f = 997.4$ kg m^{-3}, respectively. Initially the island was saturated up to $y = 0.3$ m with salt water to represent the ocean. Freshwater was recharged, with a rate equal to $q = 1.33 \times 10^{-5}$ m s^{-1}, through a set of drips above the sand cone. The recharged fresh water penetrated into the porous medium (i.e., island) and formed a freshwater lens as shown in Fig. 2. As the experiment progressed, an amount of freshwater discharged from the island to the surrounding salt water representing the ocean. This water was skimmed from the salt water surface (Fig. 2) to maintain a constant salt water level (Stoeckl and Houben, 2012).

In the simulation, a plane of symmetry was assumed requiring only half of the experimental domain to be simulated; this is similar to the numerical study performed in Stoeckl et al. (2016). The left side of the island was simulated, and a free-slip boundary condition was used on the right wall of the domain to satisfy the symmetry of the flow. The initial spacing between fluid particles ($\Delta x = \Delta y$) was set to 0.005 m in the ocean, and $0.005/\sqrt{\epsilon}$ m in the island. The smoothing length, h, was set to $1.2\Delta x$, with Δx varying in the ocean and island. The time step was set to 2×10^{-4} s. The dynamic viscosity for the fresh water was set to $\mu_f = 10^{-3}$ Pa·s and it was assumed to be $\mu_s = 1.05 \times 10^{-3}$ Pa·s for the salt water (Isdale et al., 1972). The calculated permeability was $\kappa = 4.6 \times 10^{-10}$ m^2, using the properties of freshwater and hydraulic conductivity. No-slip boundary conditions were imposed on the left and bottom solid boundaries. The longitudinal and transverse dispersivity, included in Eq. (32), were set to $d_l = 5 \times 10^{-4}$ m and $d_t = 5 \times 10^{-5}$ m, and the coefficient of molecular diffusivity was set to $D_m = 10^{-9}$ m^2 s^{-1}

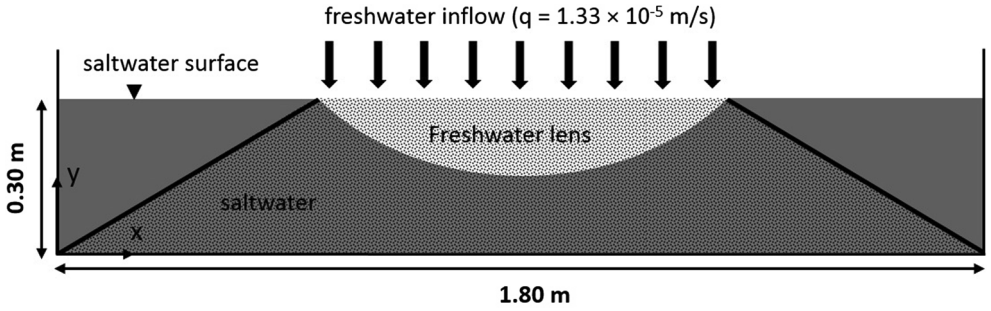

Fig. 2. The experimental tank used in Stoeckl and Houben (2012) (Section 3.1).

(Stoeckl et al., 2016). The freshwater recharge at the surface of the island was simulated using an inflow boundary condition (Section 2.5.3). The pressure within the inflow zone was set to be hydrostatic at every time step. Outside the island, particles that moved above $y = 0.3$ m, were deleted to keep the water level constant and mimic the experimental procedure.

Fig. 3 shows the freshwater lens and the pressure distribution at different times. The coarser resolution of particles in the porous medium is due to the definition of spatial volume, that changes in accordance to porosity of the medium. Experimental or numerical pressure measurements are not available and a qualitative discussion is reported here. The value of maximum pressure in the porous medium is higher than that of the free flow domain; this is due to the extra pressure imposed by the inflow particles over the surface of the island. It was found that changing the thickness of the inflow zone, which changed the hydrostatic pressure at the surface of the island accordingly, affected the maximum thickness of the lens predicted numerically. Our investigations showed that the thickness of the inflow zone should be equal to the radius of the support domain of the kernel function. The definition of pressure at inflow boundary condition in SPH is still an open issue, with examples (Nomeritae et al., 2018) showing the need to adjust the size of inflow zone to reproduce experimental data.

Oscillations in pressure values occurred at the interface between the free flow domain and the porous medium (Fig. 3). This might be due to the fact that for a support domain with its centre located right over the interface there are different numbers of particles within it from the two media. Our investigations showed that these oscillations do not significantly affect the numerical results.

It was found that with the proper boundary arrangements, the transient formation as well as the maximum thickness of the lens were reasonably reproduced. The numerical maximum thickness of the lens occurred close to the right boundary which is in agreement with the experimental and numerical results in Stoeckl and Houben (2012) and Stoeckl et al. (2016). The maximum depth predicted numerically was 16 cm and occurred in the middle of the island after 200 min; this was close to the maximum thickness measured experimentally, 15 cm, that occurred at the same time.

It is observed in Fig. 3 that the density of salt water in the free flow domain, at the interface between the free flow domain and the porous medium and close to the free surface, is lower than the salt water density. This was due to a horizontal flow within the lens, from the symmetry boundary toward the left; this was observed in the experiment (Stoeckl and Houben, 2012) and numerical benchmark by Stoeckl et al. (2016). It was also found that an amount of the discharged fresh water into the ocean moved back to the island, and again converged with the horizontal flow of lens water into the salt water surface (Fig. 3, $t = 200$ min). This represents the direction of the salt water flow from the free flow domain into the porous medium. A similar flow direction was observed in the simulation of Stoeckl et al. (2016).

It is observed that the thickness of the transition between freshwater and salt water is larger close to the symmetry boundary; likely due to the higher vertical velocity of particles close to the symmetry boundary as the effective dispersion matrix is proportional to the velocity of particles.

The simulation was repeated for four other recharge rates and the maximum lens thickness was compared to numerical and analytical solutions (Stoeckl and Houben, 2012; Fetter, 1972; Vacher, 1988) to investigate the capability of the model to predict the maximum thickness as a function of recharge rate. As observed in Fig. 4a and b, the EISPH results are in good agreement with the numerical and analytical results.

The results show that the EISPH can be used to well simulate applications associated with multi-fluid flows in porous media.

3.2. Salt water upconing in a two-dimensional aquifer

A series of experiments of salt water upconing were presented in Werner et al. (2009) and their experiment 2 was used for comparison of the simulations here. In the experiment, a tank 1.18 m long, 1.2 m deep, and 0.053 m wide was used, as shown in Fig. 5. Four pipes fed freshwater and one pipe fed salt water to the tank from both sides. The conductance (i.e., resistance of the porous medium against the inflow) was measured as $M_f = 2.84 \times 10^{-6}$ m^2 s^{-1} and $M_s = 1.62 \times 10^{-6}$ m^2 s^{-1} for the fresh water and salt water, respectively (Jakovovic et al., 2011). Initially the tank was filled up to 0.15 m with salt water and 1 m depth of fresh water was filled over the salt water leading to an overall depth $H_b = 1.15$ m (i.e., the fresh water head measured from the base of the tank). Fresh water was extracted, using an extraction well with diameter equal to 0.012 m, at the rate $Q_p = 7 \times 10^{-5}$ m^2 s^{-1}. The well was placed in the middle of the tank at a depth of 0.65 m from the top of the tank so that the distance between the well bottom to the initial interface of freshwater and salt water was 0.4 m (Jakovovic et al., 2011). The freshwater inflow to the well occurred at the lower 0.1 m of it. The porosity and hydraulic conductivity were given as $\epsilon = 0.38$ and $K = 1.6 \times 10^{-3}$ m s^{-1}, respectively. The density of the salt and fresh water were $\rho_s = 1025$ kg m^{-3} and $\rho_f = 998$ kg m^{-3}, respectively (Werner et al., 2009; Jakovovic et al., 2011). Two manometers were attached at the boundaries at both sides to measure any drawdown in the fresh water and salt water head. As the freshwater and salt water head dropped at the boundaries, an inflow was induced to feed the domain with both freshwater and salt water. Therefore, the side boundaries acted as head dependent boundaries.

In the simulation, the initial spacing between fluid particles ($\Delta x = \Delta y$) was set to $0.005/\sqrt{\epsilon}$ m. The smoothing length, h, was set to $1.2\Delta x$ and the time step was 2×10^{-4} s. The dynamic viscosity for the fresh water was set to $\mu_f = 10^{-3}$ Pa·s and it was assumed to be $\mu_s = 1.05 \times 10^{-3}$ Pa·s for salt water (Isdale et al., 1972). The calculated permeability was $\kappa = 1.67 \times 10^{-10}$ m^2, using the parameters of salt water and hydraulic conductivity. The lower section of the well (dashed zone in Fig. 5), where freshwater was flowing into, was treated as a high permeability section (i.e., the drag force in Eq. (6) was set to zero), and its length was assumed to be 0.05 m (Jakovovic et al., 2011). The sink point location was set at the middle of the permeable zone. A no-

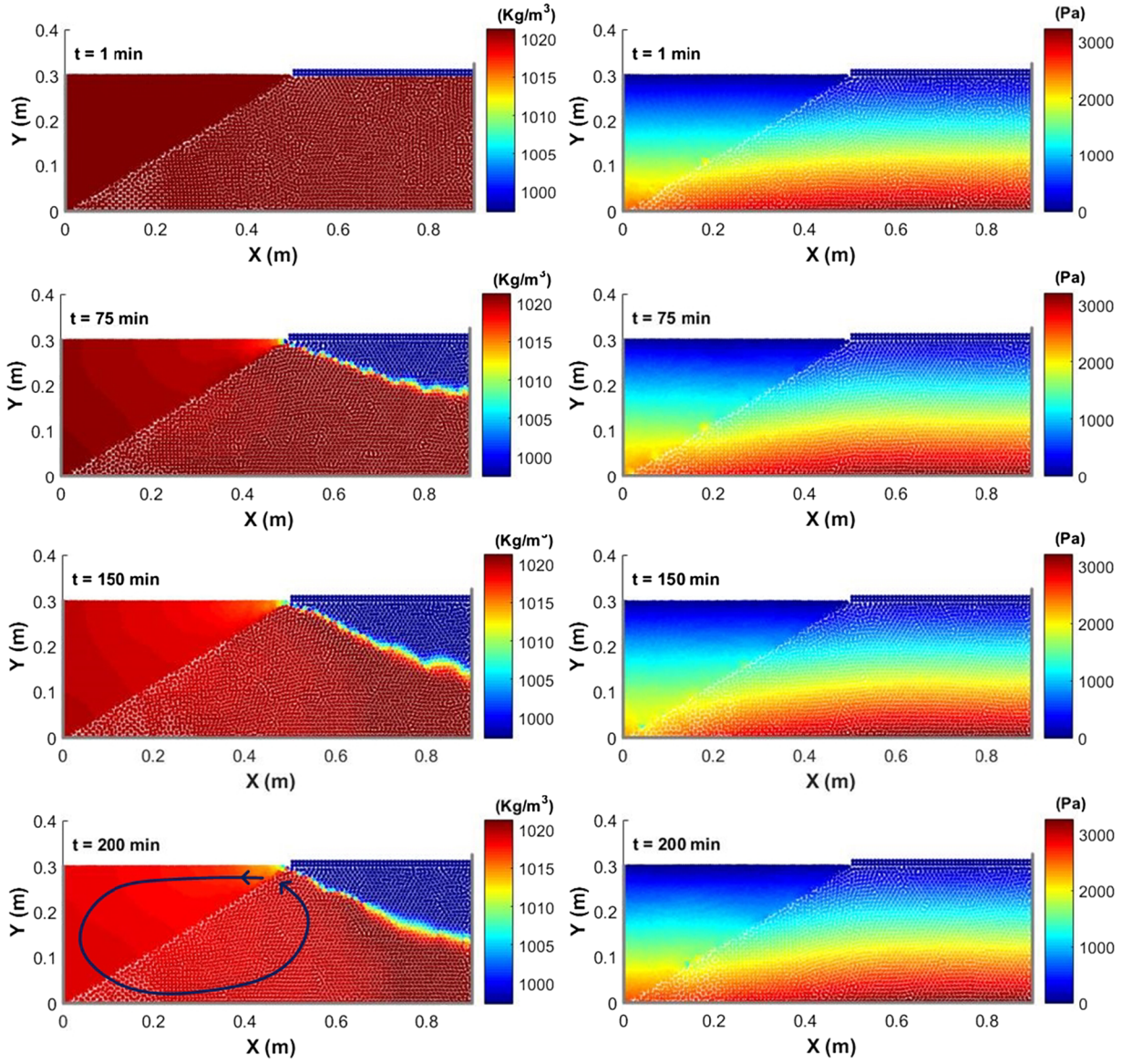

Fig. 3. Distribution of fluid density (left) and pressure (right) at different times (Section 3.1).

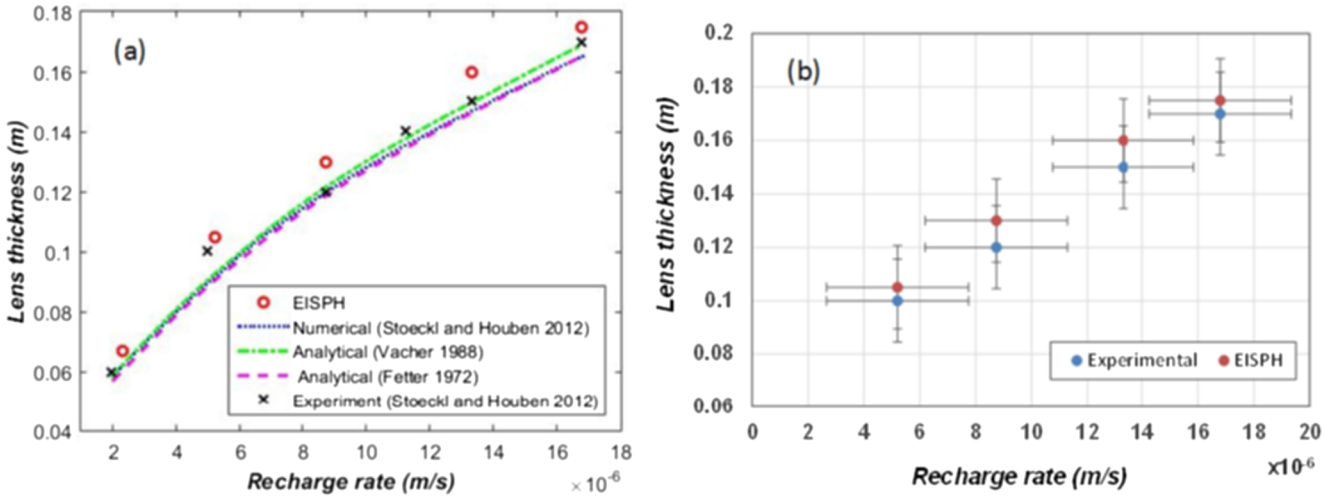

Fig. 4. (a) Comparison of the EISPH results against experimental data for maximum lens thickness as a function of recharge rate and (b) error bars for the simulations (Section 3.1).

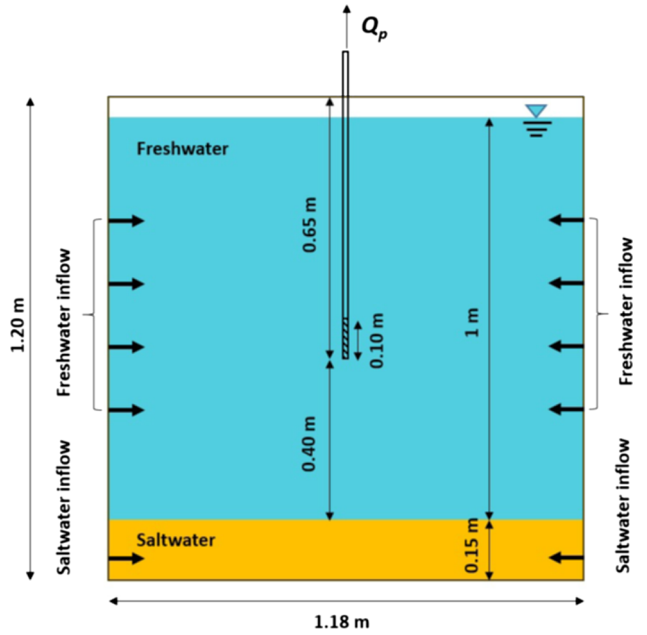

Fig. 5. The view of the tank used in the experiment by Werner et al. (2009) (Section 3.2).

slip boundary condition was imposed at the bottom solid boundary. The coefficient of molecular diffusivity was set to $D_m = 10^{-9}$ m^2 s^{-1}, and the longitudinal and transverse dispersivity were set to $d_l = 2 \times 10^{-3}$ m and $d_t = 1 \times 10^{-4}$ m (Jakovovic et al., 2011).

The fresh water and salt water recharge were simulated using an inflow boundary condition (Section 2.5.3), with the rate of the inflow determined according to the boundaries' time dependent head. The inflow was simulated as a continuously distributed recharge rather than inflow nodes or pipes. This was due to the nature of SPH, as a kernel close to the boundaries needs to be filled with particles to result in an accurate approximation. The width of the inflow zones, on the left and right boundaries, were set to 0.04 m, which was larger than the radius of the support of the kernel function. The inflow rate for fresh water, q_f (m s^{-1}), and salt water, q_s (m s^{-1}), was calculated using the conductance, initial boundary head (H_b), and time dependent internal head at the boundaries (H_t) as Jakovovic et al. (2011)

$$q_f = M_f(H_b - H_t)/(((H_b - 0.15)/4) \times 0.053), \quad (15)$$

and

$$q_s = M_s(H_b - H_t)/(0.15 \times 0.053), \quad (16)$$

where H_t was assumed to be the average of the freshwater heads on the left and right boundaries, to ensure a symmetrical inflow, as it was observed in the experiment (Werner et al., 2009).

Fig. 6 shows the density distribution and transient development of the upconing below the extraction well using the method *SPR* (See Section 2.3). In the early stages of the experiment (Werner et al., 2009), a wave-like interface rise was observed; however, this wasn't observed in our simulation. This might be due to the continuously distributed inflow conditions on the sides of the tank, because the wave-like interface rise was due to the localised circulations induced by the node inflows in the experiment (Jakovovic et al., 2011). The qualitative observation is in agreement with one of the simulations in Jakovovic et al. (2011), where a continuously distributed inflow was used.

The dispersion zone at the interface between fresh water and salt water, especially in the later stages of the simulation, was wider than the experimental dispersion zone. Our investigations showed that using a smaller values for longitudinal and transverse dispersivity did not considerably affect the dispersion zone width. A thicker dispersion zone, but with smaller extent, was also observed in the simulations of Jakovovic et al. (2011). This thicker dispersion zone might be related to the assumption in the SPH approximation of the diffusion equation (see Eqs. (31)–(34)).

Fig. 7a illustrates the upconing height as a function of time. The numerical height of the upconing was determined based on the simulated 50% salinity contour (Jakovovic et al., 2011). It was observed that the *SPR* method led to results comparatively closer to the experimental observations. Fig. 7b shows the error bar for the *SPR* method. The *CMR* method considerably overestimated the upconing heigh, possibly because of the particle distribution pattern around the sink point. Fig. 8 shows the particles around the sink point for the three sink methods. The particles have an ordered distribution around the sink point in the *SPR*, while the particles are clumped for *CMR* method. The clumping in *CMR* is due to the continuous reduction of mass for the sink particles, until their mass drops to zero. With the density of the particles around the sink point staying constant, the reduction in mass causes the particles to get closer to the sink point. Therefore, any support domain of kernel located in the vicinity of the sink area might be truncated and causes an error in the particle approximations. The clumping was also observed in the method *MRPR*, to a smaller extent especially when implementing $MRPR_K$, because particles mass were set to their initial value when a particle was removed.

The stability of the simulations and the qualitative and quantitative results show the capability of the sink algorithms to reproducing fresh water pumping in aquifers.

4. Conclusion

Application of SPH schemes to multi-fluid flows in porous media with different porosities are not very common. In this paper, an EISPH numerical scheme was used to investigate its applicability to seawater intrusion problems. The focus was on the dynamics of buoyant freshwater lenses in islands and salt water upconing caused by pumping. The model was tested against published results from laboratory experimental and models.

In the case of the freshwater lens, the transient thickness and maximum depth of the simulated lens were in reasonable agreement with experimental data. The simulated maximum depth of the lens as a function of different recharge rates were in agreement with observed, analytical and other numerical results. The imposition of flow boundary conditions to simulate recharge still represents a challenge in SPH. The lens dimensions obtained with EISPH depended on the thickness of the inflow zone, as this controlled the value of hydrostatic pressure acting on the surface of the island. This depths was thus calibrated to best reproduce experimental data. The inclusion of pumping was the main challenge to model salt water upconing. A new procedure for implementing a sink in SPH was developed. The divergence of the velocity for the particles in the vicinity of the sink point was adjusted in accordance with the pumping rate to make the particles move toward the sink. The extraction of mass was handled using three different methods indicated as *SPR*, *MRPR*, and *CMR*. *SPR*, where the mass reduction is handled solely through removal of particles, appeared to perform better when compared to experimental observations. The quantitative results of the cases studied here show the effectiveness of EISPH in simulating complex flow conditions and lay the foundation for the inclusion of mass sinks in SPH numerical schemes applied to water pumping. Although applied to 2D configurations, the algorithm developed is also applicable to 3D problems. To preserve reasonable computational times, future avenues to improve the method point toward the extension of the model to radial coordinates or, perhaps, the development of ad hoc changes of the values of permeability and porosity to generate

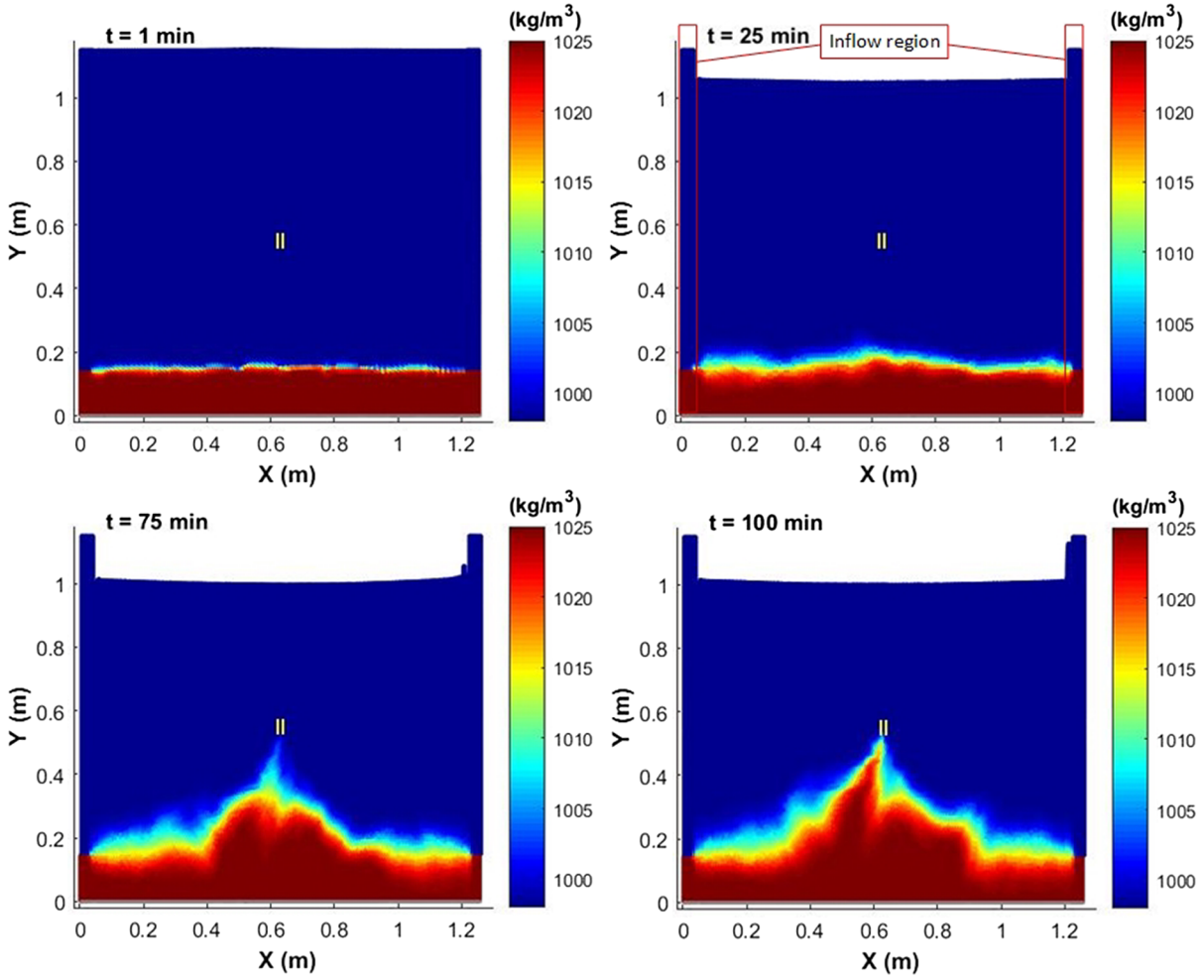

Fig. 6. Transient development of the salt water upconing below the single sink point using method *SPR* (the yellow lines, representing the bottom (high permeable) section of the well, are only shown for visualisation purpose) (Section 3.2). (For interpretation of the references to colour in this figure legend, the reader is referred to the web version of this article.)

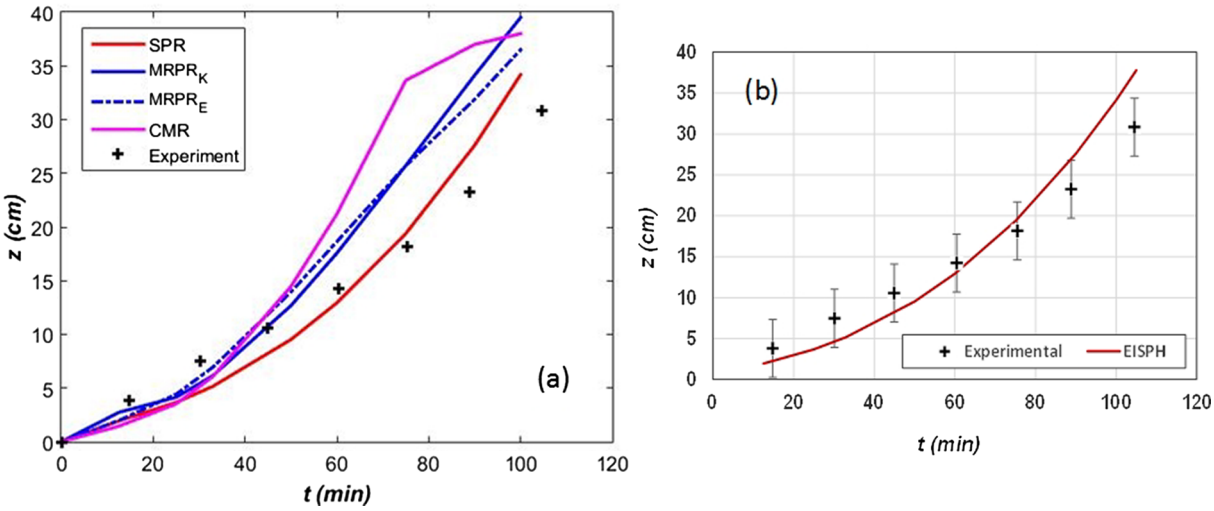

Fig. 7. (a) Comparison of upconing height, apex rise, from the observed data and numerical model and (b) error bars for the *SPR* method (Section 3.2).

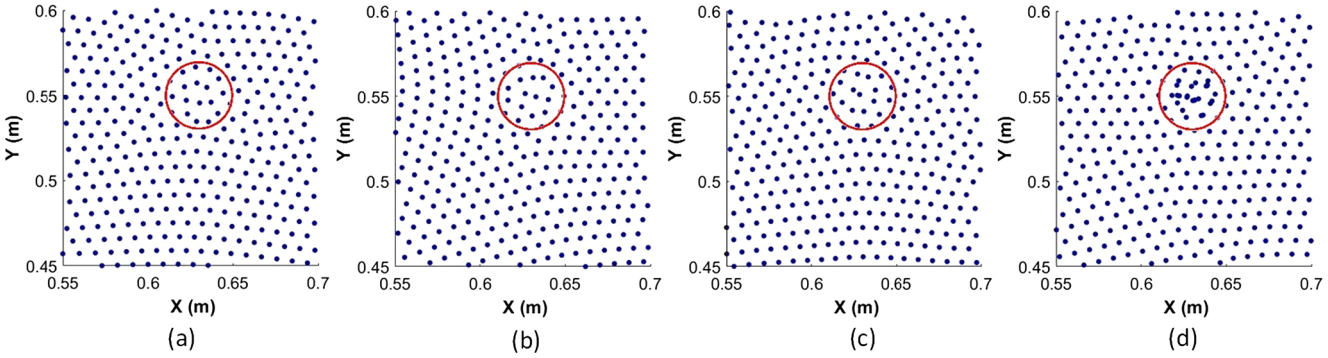

Fig. 8. The distribution of particles around the sink point, $X = 0.63$ m and $Y = 0.55$ m, for methods (a) *SPR* (b) $MRPR_E$ (c) $MRPR_K$ and (d) *CMR* (Section 3.2).

2D domains equivalent to 3D axisymmetric problems (e.g., Langevin et al., 2008).

Declaration of Competing Interest

None.

Acknowledgements

The Authors thank V. Lemiale and A. Valizadeh for useful discussions.

Appendix A. EISPH scheme

This section presents a detail description of the numerical method used to solve Eqs. (1)–(3) with SPH. The numerical scheme selected is EISPH, which has been shown to be computationally efficient and have lower pressure fluctuations when compared to other SPH schemes (Nomeritae et al., 2016). Parts of the method are also described in Basser et al. (2017).

The governing equations were solved with an EISPH scheme, which employs two steps (Cummins and Rudman, 1999). The Poisson equation is approximately solved.

In the first step, viscous, gravity and drag forces contribute to the velocity and position of particles as

$$\vec{u}_i^{*} = \vec{u}_i^{n} + \left(\frac{\mu}{\rho}\nabla^2\vec{u}\right)_i^n \Delta t + \epsilon_i^n \left(\vec{g} - \frac{\mu}{\rho\kappa}\vec{u}\right)_i^n \Delta t, \tag{17}$$

where $\vec{u}^{*}$ is intermediate velocity, $\vec{u}^{n}$ is particle velocity at time $n\Delta t$, with Δt kept constant in all the simulations.

The approximation of the viscous term reads

$$\left(\frac{\mu}{\rho}\nabla^2\vec{u}\right)_i^n = \sum_{j=1}^{N} \frac{4m_j^n(\mu_i + \mu_j)\vec{u}_{ij}^{n}\cdot\vec{x}_{ij}^{n}}{\epsilon_j^n\,(\rho_i^n + \rho_j^n)^2(|\vec{x}_{ij}^{n}|^2 + \eta^2)}\nabla_i W_{ij}^n, \tag{18}$$

where η is a small parameter included to make sure the denominator is non-zero ($\eta = 0.001h_{ij}$, with $h_{ij} = (h_i + h_j)/2$), and $\vec{u}_{ij}^{n} = \vec{u}_i^{n} - \vec{u}_j^{n}$. The gravitational acceleration and the drag term are explicitly calculated.

The intermediate particle positions ($\vec{x}^{*}$) are calculated as

$$\vec{x}_i^{*} = \vec{x}_i^{n} + \frac{\vec{u}_i^{*}}{\epsilon^n}\Delta t, \tag{19}$$

where $\vec{x}^{n}$ is particle position at time $n\Delta t$. Afterwards, the intermediate porosity of particles, ϵ^{*}, are assigned using the intermediate position of particles.

In the second step, the particle velocities are calculated at the new time step as

$$\vec{u}_i^{n+1} = \vec{u}_i^{*} - \frac{\epsilon_i^{*}}{\rho_i^n}\nabla p_i^{n+1}\Delta t, \tag{20}$$

where p^{n+1} is particle pressure at time $(n + 1)\Delta t$. Eqs. (20) and (1) are combined to form the pressure Poisson equation as

$$\nabla\cdot\left(\frac{\epsilon^{*}}{\rho^n}\nabla p^{n+1}\right)_i = \left(\frac{\nabla\cdot\vec{u}^{*} + \Gamma}{\Delta t}\right)_i, \tag{21}$$

where Γ is the contribution of the sink points around particle i (see Section 2.3).

The approximation of the divergence of the intermediate velocity reads

$$(\nabla\cdot\vec{u}^{*})_i = \sum_{j=1}^{N} \frac{m_j^n}{\epsilon_j^{*}\,\rho_j^n}(\vec{u}_j^{*} - \vec{u}_i^{*})\cdot\nabla_i W_{ij}^{*}. \tag{22}$$

The left hand side of Eq. (21) is a Laplacian operator and is approximated as

$$\nabla\cdot\left(\frac{\epsilon^{*}}{\rho^n}\nabla p^{n+1}\right)_i = \sum_{j=1}^{N} \frac{m_j^n}{\epsilon_j^{*}\,\rho_i^n\rho_j^n}\frac{(\epsilon_i^{*} + \epsilon_j^{*})\vec{x}_{ij}^{*}\cdot\nabla_i W_{ij}^{*}}{|\vec{x}_{ij}^{*}|^2 + \eta^2}(p_i^{n+1} - p_j^{n+1}), \tag{23}$$

so that

$$\sum_{j=1}^{N} \frac{m_j^n}{\epsilon_j^* \rho_i^n \rho_j^n} \frac{(\epsilon_i^* + \epsilon_j^*)\vec{x}_{ij}^* \cdot \nabla_i W_{ij}^*}{|\vec{x}_{ij}^*|^2 + \eta^2} (p_i^{n+1} - p_j^{n+1}) = \left(\frac{\nabla \cdot \vec{u}^* + \Gamma}{\Delta t} \right)_i. \tag{24}$$

Eq. (24) is written for particle i as

$$p_i^{n+1} = \frac{B_i + \sum_{j=1}^{N} A_{ij} p_j^{n+1}}{\sum_{j=1}^{N} A_{ij}}, \tag{25}$$

with

$$A_{ij} = \frac{m_j^n}{\epsilon_j^* \rho_i^n \rho_j^n} \frac{(\epsilon_i^* + \epsilon_j^*)\vec{x}_{ij}^* \cdot \nabla_i W_{ij}^*}{|\vec{x}_{ij}^*|^2 + \eta^2}, \tag{26}$$

and

$$B_i = \left(\frac{\nabla \cdot \vec{u}^* + \Gamma}{\Delta t} \right)_i. \tag{27}$$

Eq. (25) is explicitly solved with an approximation that has been proven to lead to satisfactory results in flow in porous media (Basser et al., 2017) as well as other applications (Nomeritae et al., 2016; Nomeritae et al., 2018). It is assumed that the value of p_j^{n+1} on the right hand side of Eq. (25) is equal to p_j^n; this is a reasonable assumption as the time step is set to a sufficiently small value. In addition, the pressure field in the cases studied here does not change considerably. The pressure of each particle is thus approximated explicitly as

$$p_i^{n+1} = \frac{B_i + \sum_{j=1}^{N} A_{ij} p_j^n}{\sum_{j=1}^{N} A_{ij}}. \tag{28}$$

The pressure of free surface particles are set to zero. The calculated pressure values are used to calculate the pressure gradient as

$$\left(\frac{\epsilon^*}{\rho^n} \nabla p^{n+1} \right)_i = \epsilon_i^* \sum_{j=1}^{N} \frac{m_j^n}{\epsilon_j^*} \left(\frac{p_i^{n+1}}{\rho_i^{n2}} + \frac{p_j^{n+1}}{\rho_j^{n2}} \right) \nabla_i W_{ij}^*. \tag{29}$$

Afterwards, the velocity field at the new time step is calculated using Eq. (20). The new position is calculated as

$$\vec{x}_i^{n+1} = \vec{x}_i^n + \frac{\left(\frac{\vec{u}_i^n}{\epsilon_i^n} \right) + \left(\frac{\vec{u}_i^{n+1}}{\epsilon_i^*} \right)}{2} \Delta t, \tag{30}$$

and new particle porosity, ϵ^{n+1}, is assigned. The particle concentration is calculated using Eq. (3) as

$$C_i^{n+1} = C_i^n + (\nabla \cdot (\mathscr{D}_d^{n+1} \nabla C))_i \Delta t, \tag{31}$$

where the effective dispersion matrix, $\mathscr{D}_d$, is determined as Salamon et al. (2006) and Avesani et al. (2015)

$$\mathscr{D}_{di}^{n+1} = \mathscr{D}_{ei}^{n+1} I + d_{ti} |\vec{u}_i^{n+1}| I + (d_{li} - d_{ti}) \frac{\vec{u}_i^{n+1} \otimes \vec{u}_i^{n+1T}}{|\vec{u}_i^{n+1}|}, \tag{32}$$

where d_l and d_t are longitudinal and transversal dispersivity, I is identity matrix of size 2, and $\mathscr{D}_e$ is effective diffusivity coefficient. In a saturated porous medium, $\mathscr{D}_e$ can be written as Simunek and Suarez (1993)

$$\mathscr{D}_{ei}^{n+1} = D_{mi} \times (\epsilon_i^{n+1})^{4/3}, \tag{33}$$

where D_m is the coefficient of molecular diffusivity.

$\mathscr{D}_d$ in Eq. (32) is a non-diagonal matrix leading to complications with the SPH approximation (Tran-Duc et al., 2016). To simplify the approximation procedure, $\mathscr{D}_d$ is reasonably assumed to be a diagonal matrix. The contribution of terms associated with non-diagonal elements of the dispersion matrix in Eq. (32) were checked in one time step and was found to be nearly three times smaller than the contribution of the diagonal elements in the cases studied here. The variation of concentration is approximated as Tran-Duc et al. (2016)

$$(\nabla \cdot (\mathscr{D}_d^{n+1} \nabla C))_i = 2 \sum_{j=1}^{N} \frac{m_j^n}{\epsilon_j^{n+1} \rho_j^n} \left(\frac{e_{ij,1}^2}{\bar{\mathscr{D}}_{d\,ij,11}^{n+1}} + \frac{e_{ij,2}^2}{\bar{\mathscr{D}}_{d\,ij,22}^{n+1}} \right)^{-1} \frac{\vec{x}_{ij}^{n+1} \cdot \nabla_i W_{ij}^*}{|\vec{x}_{ij}^{n+1}|^2 + \eta^2} (C_i^n - C_j^n), \tag{34}$$

where $e_{ij} = \vec{x}_{ij}/|\vec{x}_{ij}|$ is the unit vector from i to j, and $\bar{\mathscr{D}}_{d\,ij}$ is the average of the elements in the effective dispersion matrices of particles i and j. Afterwards, the particles density and mass are calculated as Pahar and Dhar (2016)

$$\rho_i^{n+1} = C_i^{n+1}(\rho_s - \rho_f) + 0.5(\rho_s + \rho_f), \tag{35}$$

$$m_i^{n+1} = \rho_i^{n+1} V_{pi}^{n+1}, \tag{36}$$

where V_p is volume of fluid a particle carries and is equal to $V_p = m_j/\rho_j$.

The time step value, Δt, is defined to satisfy the Courant stability and viscous diffusion conditions as

$$\Delta t \leqslant min(\Delta t_{CFL}, \Delta t_{visc}), \tag{37}$$

with

$$\Delta t_{CFL} \leqslant 0.25 \frac{h}{u_{max}}, \tag{38}$$

and

$$\Delta t_{visc} \leqslant 0.125 \frac{h^2}{\nu}, \tag{39}$$

where ν is the kinematic viscosity and u_{max} is the maximum velocity predicted in the computations (Morris et al., 1997).

References

Avesani, D., Herrera, P., Chiogna, G., Bellin, A., Dumbser, M., 2015. Smooth particle hydrodynamics with nonlinear moving-least-squares weno reconstruction to model anisotropic dispersion in porous media. Adv. Water Resour. 80, 43–59.

Avesani, D., Dumbser, M., Chiogna, G., Bellin, A., 2017. An alternative smooth particle hydrodynamics formulation to simulate chemotaxis in porous media. J. Math. Biol. 74 (5), 1037–1058.

Basser, H., Rudman, M., Daly, E., 2017. SPH modelling of multi-fluid lock-exchange over and within porous media. Adv. Water Resour. 108, 15–28.

Bear, J., Bachmat, Y., 2012. Introduction to Modeling of Transport Phenomena in Porous Media, vol. 4 Springer Science & Business Media.

Bertorelle, E., 2014. Laboratory Experiments on the Saltwater Intrusion Process. University of Padua. URL:http://tesi.cab.unipd.it/46841/1/Tesi_Bertorelle.pdf.

Cummins, S.J., Rudman, M., 1999. An SPH projection method. J. Comput. Phys. 152 (2), 584–607.

Dagan, G., Bear, J., 1968. Solving the problem of local interface upconing in a coastal aquifer by the method of small perturbations. J. Hydraul. Res. 6 (1), 15–44.

Federico, I., Marrone, S., Colagrossi, A., Aristodemo, F., Antuono, M., 2012. Simulating 2d open-channel flows through an SPH model. Eur. J. Mech.-B/Fluids 34, 35–46.

Fetter, C., 1972. Position of the saline water interface beneath oceanic islands. Water Resour. Res. 8 (5), 1307–1315.

Herrera, P.A., Massabó, M., Beckie, R.D., 2009. A meshless method to simulate solute transport in heterogeneous porous media. Adv. Water Resour. 32 (3), 413–429.

Isdale, J., Spence, C., Tudhope, J., 1972. Physical properties of sea water solutions: viscosity. Desalination 10 (4), 319–328.

Jakovovic, D., Werner, A.D., Simmons, C.T., 2011. Numerical modelling of saltwater upconing: comparison with experimental laboratory observations. J. Hydrol. 402 (3), 261–273.

Langevin, C.D., Thorne Jr, D.T., Dausman, A.M., Sukop, M.C., Guo, W., 2008. Seawat Version 4: A Computer Program for Simulation of Multi-species Solute and Heat Transport (Tech. rep.). Geological Survey (US).

Liu, G.-R., Liu, M.B., 2003. Smoothed Particle Hydrodynamics: A Meshfree Particle Method. World Scientific.

Marrone, S., Antuono, M., Colagrossi, A., Colicchio, G., Le Touzé, D., Graziani, G., 2011. δ-SPH model for simulating violent impact flows. Comput. Methods Appl. Mech. Eng. 200 (13), 1526–1542.

Monaghan, J.J., 1992. Smoothed particle hydrodynamics. Ann. Rev. Astron. Astrophys. 30, 543–574.

Monaghan, J.J., 1994. Simulating free surface flows with SPH. J. Comput. Phys. 110 (2), 399–406.

Monaghan, J.J., 2005. Smoothed particle hydrodynamics. Rep. Prog. Phys. 68 (8), 1703.

Monaghan, J., 2012. Smoothed Particle Hydrodynamics and its diverse applications. Annu. Rev. Fluid Mech. 44, 323–346.

Monaghan, J.J., Huppert, H.E., Worster, M.G., 2005. Solidification using smoothed particle hydrodynamics. J. Comput. Phys. 206 (2), 684–705.

Morris, J.P., Fox, P.J., Zhu, Y., 1997. Modeling low Reynolds number incompressible flows using SPH. J. Comput. Phys. 136 (1), 214–226.

Nomeritae, Daly, E., Grimaldi, S., Bui, H.H., 2016. Explicit incompressible SPH algorithm for free-surface flow modelling: a comparison with weakly compressible schemes. Adv. Water Resour. 97, 156–167.

Nomeritae, N., Bui, H.H., Daly, E., 2018. Modeling transitions between free surface and pressurized flow with smoothed particle hydrodynamics. J. Hydraul. Eng. 144 (5).

Pahar, G., Dhar, A., 2016. Modeling free-surface flow in porous media with modified incompressible SPH. Eng. Anal. Boundary Elem. 68, 75–85.

Pahar, G., Dhar, A., 2016. Mixed miscible-immiscible fluid flow modelling with incompressible SPH framework. Eng. Anal. Boundary Elem. 73, 50–60.

Pahar, G., Dhar, A., 2017. On modification of pressure gradient operator in integrated ISPH for multifluid and porous media flow with free-surface. Eng. Anal. Boundary Elem. 80, 38–48.

Price, D.J., Monaghan, J., 2004. Smoothed particle magnetohydrodynamics–ii. Variational principles and variable smoothing-length terms. Mon. Not. R. Astron. Soc. 348 (1), 139–152.

Rafiee, A., Manzari, M., Hosseini, M., 2007. An incompressible SPH method for simulation of unsteady viscoelastic free-surface flows. Int. J. Non-Linear Mech. 42 (10), 1210–1223.

Salamon, P., Fernàndez-Garcia, D., Gómez-Hernández, J.J., 2006. A review and numerical assessment of the random walk particle tracking method. J. Contam. Hydrol. 87 (3–4), 277–305.

Simunek, J., Suarez, D.L., 1993. Modeling of carbon dioxide transport and production in soil: 1. Model development. Water Resour. Res. 29 (2), 487–497.

Stoeckl, L., Houben, G., 2012. Flow dynamics and age stratification of freshwater lenses: experiments and modeling. J. Hydrol. 458, 9–15.

Stoeckl, L., Walther, M., Graf, T., 2016. A new numerical benchmark of a freshwater lens. Water Resour. Res. 52 (4), 2474–2489.

Tran-Duc, T., Bertevas, E., Phan-Thien, N., Khoo, B.C., 2016. Simulation of anisotropic diffusion processes in fluids with smoothed particle hydrodynamics. Int. J. Numer. Meth. Fluids 82 (11), 730–747.

Vacher, H., 1988. Dupuit-ghyben-herzberg analysis of strip-island lenses. Geol. Soc. Am. Bull. 100 (4), 580–591.

Voss, C.I., Provost, A.M., G.S. (U.S.). Sutra, A Model for Saturated-Unsaturated, Variable-density Ground-water Flow with Solute or Energy Transport, U.S. Dept. of the Interior, U.S. Geological Survey Reston, Va.

Werner, A.D., Jakovovic, D., Simmons, C.T., 2009. Experimental observations of saltwater up-coning. J. Hydrol. 373 (1), 230–241.

Werner, A.D., Bakker, M., Post, V.E., Vandenbohede, A., Lu, C., Ataie-Ashtiani, B., Simmons, C.T., Barry, D.A., 2013. Seawater intrusion processes, investigation and management: recent advances and future challenges. Adv. Water Resour. 51, 3–26.

Werner, A.D., Sharp, H.K., Galvis, S.C., Post, V.E., Sinclair, P., 2017. Hydrogeology and management of freshwater lenses on atoll islands: review of current knowledge and research needs. J. Hydrol. 551, 819–844.

White, I., 1996. Fresh Groundwater Lens Recharge, Bonriki, Kiribati. UNESCO, Paris.